Check for updates

Synthesis and characterizations of natural limestone-derived nano-hydroxyapatite (HAp): a comparison study of different metals doped HAps on antibacterial activity†

Karya Sinulingga,[a] Makmur Sirait, (ID) *[a] Nurdin Siregar[a] and Hairus Abdullah (ID) [b]

Earth-abundant mineral limestone obtained from North Sumatera, Indonesia, has been utilized to synthesize nano-hydroxyapatite (HAp). Although HAp is biocompatible to the human bone, its antibacterial activity is still very low. Herein, different metal ions (*i.e.*, Ag, Cu, Zn, and Mg) were doped into HAp to improve the antibacterial activity. The as-synthesized HAp was characterized by X-ray ray diffraction (XRD), field-emission scanning electron microscope (FE-SEM), energy disperse spectroscopy (EDS), Fourier transmission infrared spectroscopy (FTIR), X-ray photoelectron spectroscopy (XPS), and Brunauer–Emmett–Teller (BET). The antibacterial test showed that the performance of HAp to inactivate bacterial growth was significantly improved after incorporating the metal ion dopants into HAp. Ag-HAp exhibited the highest activity toward *E. coli* and *S. aureus* with an antibacterial rate of 99.9 $\pm$ 0.1%, followed by Zn-HAp, Cu-HAp, and Mg-HAp.

1. Introduction

Hydroxyapatite (HAp) is one of the bioceramics that has been intensively studied, especially related to medical applications.[1] The extension of its application is inseparable from the importance of hydroxyapatite properties, including being bio-resorbable, osteoconductive, biocompatible, and non-toxic.[2] HAp is still being developed to further improve its applications. Recently, HAp has been widely used as a drug delivery system, for coating implants, and as scaffolding for tissue engineering. HAp is well known to not only be biocompatible but also have an osteoconductive property to natural human bone.[3,4] Furthermore, HAp is also widely used in the dentistry field for treating periodontal defects, dental implant coatings, and filler restoration materials.[5] HAp consists of calcium, phosphate, and hydroxide groups with the leading chemical formula of $Ca_{10}(PO_4)_6(OH)_2$.[6] It can be synthesized by mixing synthetic chemicals such as $CaCl_2$, $Ca(NO_3)_2$, $Ca(OH)_2$, *etc.* and phosphate precursors such as H_3PO_4 and $(NH_4)H_2PO_4$ during the fabrication process.[6–8] The raw materials for producing hydroxyapatite can also be obtained from natural sources. Some previous studies examined hydroxyapatite manufacturing using natural calcium sources such as clamshell[9] and eggshell,[10] but their

availability is limited. Therefore, the synthesis of HAp by utilizing earth-abundant sources is critical. Limestone, one of the most abundant minerals on earth, possesses high calcium content of about 40.04 at%.[11] Thus, it can be used as a source for the synthesis of large-scale HAp powder. The synthesis method has a vital role in determining the morphology, crystal structure, and purity of the HAp.[12] Its crystal structure can be either monoclinic or hexagonal, depending on the synthesis method. The monoclinic system only can be obtained with a stoichiometric composition of Ca/P ratio of 1.67. In contrast, the hexagonal structure is obtained from a non-stoichiometric composition. In the last few years, nanoscale hydroxyapatite particles have been synthesized and developed. Nano-hydroxyapatite with particle size less than 100 nm could provide a higher surface area and more biocompatible to human bone tissue.

Although HAp is well known to be biocompatible to human tissue, its mechanical properties and antibacterial activity are still lacking. These disadvantages of HAp should be overcome before being implemented for actual applications. Some researchers have successfully improved the mechanical properties of HAp by adding fillers such as ZnO,[13] zirconia,[14] carbon nanotube,[15] and chitosan.[16] On the other hand, the antibacterial capability of HAp is another significant property for bone grafts and dental implant applications to prevent infections after surgery.[17] Doping with metal ions is the most powerful strategy to improve the antibacterial activity of HAp.[18] Several metal doping ions had been used in the previous reports to enhance the antibacterial activity of HAp, such as silver (Ag^+), zinc (Zn^{2+}),

[a]Department of Physics, Faculty of Mathematics and Natural Sciences, Universitas Negeri Medan, 20221, Indonesia. E-mail: maksir@unimed.ac.id

[b]Department of Industrial Engineering, Universitas Prima Indonesia, Medan, Indonesia

magnesium (Mg^{2+}), and copper (Cu^{2+}) ions.[19–21] Among them, silver is the most widely explored due to its high antibacterial activity.[22]

Based on the above considerations, hydroxyapatite synthesis and characterization by utilizing earth-abundant limestone resources are highly critical. Although there are several reports on studying the synthesis and antibacterial activity of HAp[23–25] but in this report, we comprehensively synthesized and compared the effect of metal ions dopant on the antibacterial activity of HAp. To the best of our knowledge, no report compares antibacterial of HAp with different metal ions dopant using natural Sidikalang limestone as the calcium source. The as-synthesized un-doped and metal ions doped HAp were systematically characterized using several techniques such as XRD, FE-SEM, FTIR, XPS, and BET to investigate their properties. Further, the antibacterial experiments show that all metal ions doped-HAp perform much higher antibacterial than un-doped HAp with activity order Ag- > Zn- > Cu- > Mg-doped HAp > pristine HAp.

2. Experimental section

2.1 Synthesis HAp and M doped HAp

Fig. 1 schematically shows the synthesis process of HAp from the natural limestone. In detail, natural limestone was firstly heated at 900 °C for 5 hours in an electric furnace to convert it into CaO. This CaO was then used as the calcium source to synthesize HAp. The HAp was synthesized by dissolving 5.6 g CaO into 500 mL deionized (DI) water under constant stirring for several hours to form $Ca(OH)_2$. Then, 3.1 mL phosphoric acid (H_3PO_4, J. T Baker, Mexico) was added into the solution and continuously stirred for 12 h. Finally, the obtained precipitation was dried and annealed at 700 °C for 2 h to obtain pristine HAp. A similar procedure synthesized the other samples with Ag-, Cu-, Zn-, and Mg-doped HAp by adding 5% of metal ion precursors ($AgNO_3$, $Cu(NO_3)_2$, $Zn(NO_3)_2$, and $Mg(NO_3)_2$) during the preparation process before the additional of 3.1 mL phosphoric acids. The as-prepared metal ion-doped HAps were denoted as Ag-HAp, Cu-HAp, Zn-HAp, and Mg-HAp in the data presented.

2.2 Characterizations

The X-ray diffraction (XRD, D2 Phaser, Bruker, Karlsruhe, Germany) was used to identify the crystal structure of un-doped HAp and metal ion-doped HAp. The morphology was recorded using a field-emission scanning electron microscope (FE-SEM, JSM 6500F, JEOL, Tokyo, Japan). The element composition was investigated by an electron dispersive spectroscopy (EDS) and analyzed using integrated calibration and application tool (INCA software, Oxford instrument, Abingdon, UK). An infrared spectrophotometer (FTS1000, Digilab, USA) was used to confirm the functional group of HAp. Moreover, the specific surface areas of un-doped HAp and different metal ions-doped HAp powders were measured with a Brunauer–Emmet–Teller (BET) nitrogen adsorption method. The nitrogen adsorption and desorption isotherms were generated at 77.15 K on a constant-volume adsorption apparatus (Novatouch LX2, Quantachrome Instrument, Boyton Beach, FL, USA). The X-ray photoelectron spectroscopy (VG Scientific ESCALAB) was carried out to study the chemical composition of un-doped HAp and different metal ions-doped HAp.

2.3 Antibacterial activity

In this study, all samples' antibacterial activities were tested toward *Escherichia coli* (*E. coli*) bacteria (DH5-Alpha) and *Streptococcus aureus* (*S. aureus*) bacteria (ATCC 25175). The bacterial activity was evaluated based on the plate count technique (ASTM International E3031-15) with quantitative bacteria colonies on a Petri dish, similar to the previous report.[20] The initial bacteria were inoculated overnight in Luria–Bertani medium at 37 °C. The concentration of bacteria was diluted in phosphate-buffered saline solution and 1 mg of pristine and metal ions doped HAp samples were added to 0.5 mL diluted bacteria solution (10^3 colony-forming unit, CFU). Subsequently, the 0.5 mL bacteria solution was spread on agar medium on a Petri dish. Finally, the Petri dish was transferred to an incubator and cultured at 37 °C for 20–24 h. The amounts of bacteria were counted by colony counter machine (Rocker galaxy 330, Kaohsiung, Taipei) and the results were compared with the control sample (pure bacteria). The antibacterial activity was calculated based on the colony numbers and determined with an equation as follows:

$$R = [(A - B)/A] \times 100\%$$

Where R is the antibacterial rate (%), A is the average number of bacteria (CFU) on control without any HAp sample, and B is the average number of bacteria (CFU) on the testing sample with pristine HAp and metal ions-doped HAp. The antibacterial activity of each sample is determined by triplicate measurements. The means and standard deviations of the antibacterial rate were calculated using Origin Pro Software (Origin Lab Corporation).

Fig. 1 Synthesis steps of HAp from natural limestone-extracted CaO.

3. Results and discussion

3.1 Crystal analysis

XRD analysis was carried out to study the crystal properties of as-synthesized hydroxyapatite, including the phase transformation, crystal structure, lattice parameters, and estimated crystallite size. Fig. 2 shows the X-ray diffraction patterns of as-synthesized HAp from Sidikalang natural limestone with different metal ion dopants. The X-ray diffraction pattern of pristine HAp is similar to standard ICDD-PDF no. 9-432. The 2θ peaks that located at 31.77°, 32.19°, 32.90°, 34.05°, 35.48°, 39.20°, 39.82°, 42.03°, 43.80°, 45.30°, 46.71°, 48.10°, 48.62°, and 49.45° are related to (211), (112), (300), (301), (212), (310), (311), (113), (203), (222), (312), (320), and (213) planes, respectively. There is a slight peak-shift to a higher angle than the standard file due to a smaller lattice parameter. The XRD pattern of Ag-doped HAp shows several new peaks compared to that of pristine HAp which corresponds to the formation of secondary phases. The peaks located at 31.30° and 34.60° (assigned with symbol *) correspond to beta-tricalcium phosphate (β-TCP) based on ICDD-PDF no. 9-169. Interestingly, the formation of HAp and β-TCP, known as biphasic calcium phosphate, is also suitable for bone implants. The appearance of phase separation was also found in the previous reports.[26,27] The other two new peaks at 38.40° and 44.50° could be assigned as the presence of Ag metal according to the ICDD-PDF no. 4-783. The finding for Ag-HAp was consistent with the previous report.[24,27] The metallic Ag presence could be explained as the processing temperature is high, then Ag⁺ ions migrate into bulk and reduced into Ag metal.[28] The fact of β-TCP is elaborated as follows. In the preparation stage, we designed the ratio of (Ca + Ag)/P = 1.67. Since the Ag⁺ ions did not dope into Ca²⁺ sides, then the ratio of Ca/P became lower and resulted from β-TCP
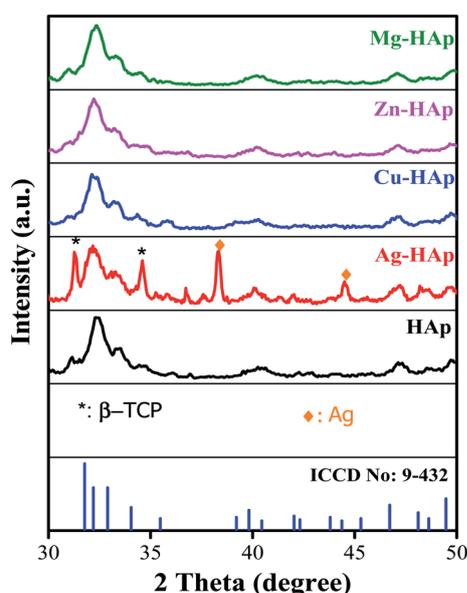
Table 1 FWHM and Crystallite sizes of un-doped, Ag-, Cu-, Zn-, and Mg-doped HAp

Samples	FWHM	Crystallite size (nm)
HAp	0.543	15.1
Ag-HAp	0.724	11.3
Cu-HAp	0.699	11.7
Zn-HAp	0.608	13.5
Mg-HAp	0.727	11.3

with a lower Ca/P value of 1.5. However, the XRD pattern of other metal ions doping (Cu, Zn, and Mg) did not show any new peak, indicating that those metal ions had been successfully doped into HAp host lattice and formed a single phase of HAp. There is no apparent peak shift of metal ions-doped HAp to a higher or lower angle compared to that pristine HAp may due to pretty low concentration of those metal ions (about 1–2 at%) as further discuss in the next section. The FWHM and crystallite size of un-doped and doped HAp were estimated and calculated using the Scherer equation. As listed in Table 1, the crystallite size values were 15.1, 11.3, 11.7, 13.5, and 11.3 nm with FWHM values were 0.543, 0.736, 0.608, 0.756, and 0.727 for un-doped, Ag-, Cu-, Zn-, and Mg-doped HAp, respectively. The crystallite size of HAp slightly decreased after doping with different metal ions.

3.2 SEM analysis

The scanning electron microscopy analysis was carried out to evaluate the morphology and microstructures of pristine HAp and different metal ions-doped HAp. As shown in Fig. 3a, the morphology of un-doped HAp is nanoparticle with an average diameter of about 50–100 nm. There is no significant difference in SEM morphology of HAps before and after doped with different metal ion dopants. However, the particle size of HAp becomes smaller after doped with other metal ion dopants. The average diameters of un-doped, Ag-, Cu-, Zn-, and Mg-doped HAp were 57.59 ± 15.77, 40.57 ± 14.63, 42.80 ± 13.46, 38.85 ± 13.82, and 40.40 ± 14.91 nm, respectively. Furthermore, the SEM images of all metal ions-doped HAp exhibit a clear image compared to that un-doped HAp due to a better electrical conduction.[29] This result further confirms the success of metal ions doped into the HAp host lattice.

3.3 XPS analyses

XPS analysis was conducted to analyze the surface chemistry and element composition of pristine and metal ions doped HAp. The high resolution of pristine HAp is presented in Fig. 4a–c, while the high resolution of metal ions dopant for doped HAp is shown in Fig. 4d–f. Fig. 4a exhibits the high-resolution XPS of Ca 2p with the appearance of two peaks located at 347.9 and 351.5 eV, which correspond to the spin–orbit of $2p_{3/2}$ and $2p_{1/2}$, respectively.[30] The asymmetric peak of O 1s in Fig. 4b can be deconvoluted into two peaks. The peak at 532.4 eV is assigned as the O bond with P in the phosphate group.[31] Another weak peak of oxygen at 529.8 eV typically
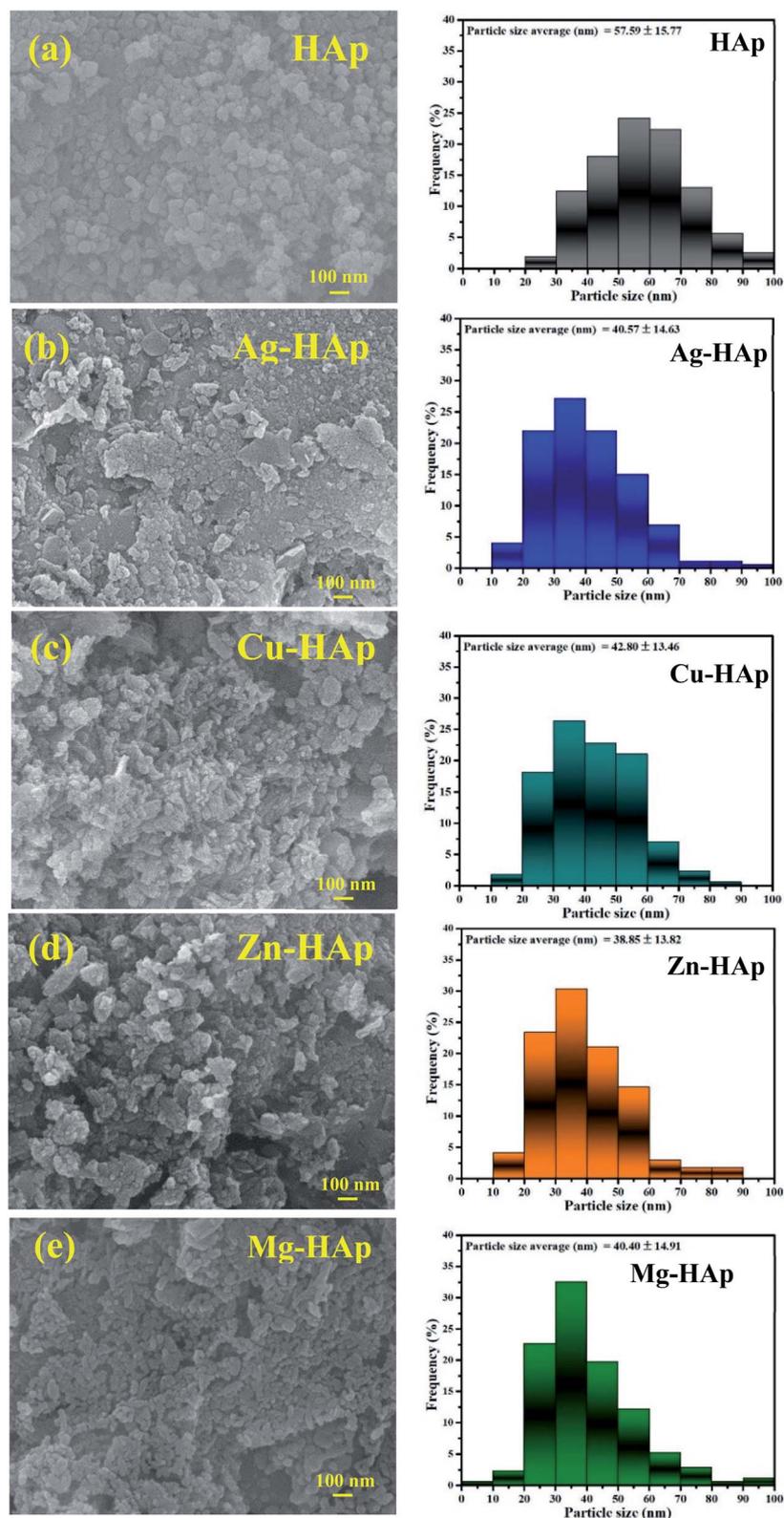

Fig. 2 X-ray diffraction patterns of un-doped, Ag-, Cu-, Zn-, and Mg-doped HAp.

© 2021 The Author(s). Published by the Royal Society of Chemistry

Fig. 3 SEM images of (a) pristine, (b) Ag-, (c) Cu-, (d) Zn-, and (e) Mg-doped HAps with their particle size distribution.

indicates the bonding of oxygen with Ca.[32] The binding energies of P $2p_{3/2}$ and P $2p_{1/2}$ are located at 133.0 and 134.0 eV, respectively,[33] as depicted in Fig. 4c. The high resolution of Ag in Ag-HAp is presented in Fig. 4d. The binding energies of 369.0 eV and 375.0 eV for spin-orbital $3d_{5/2}$ and $3d_{3/2}$ confirm the presence of metallic Ag with zero oxidation state.[34] This data agrees with the XRD result in the previous section. The high-resolution XPS of Cu 2p (Fig. 4e) for Cu-HAp shows four peaks
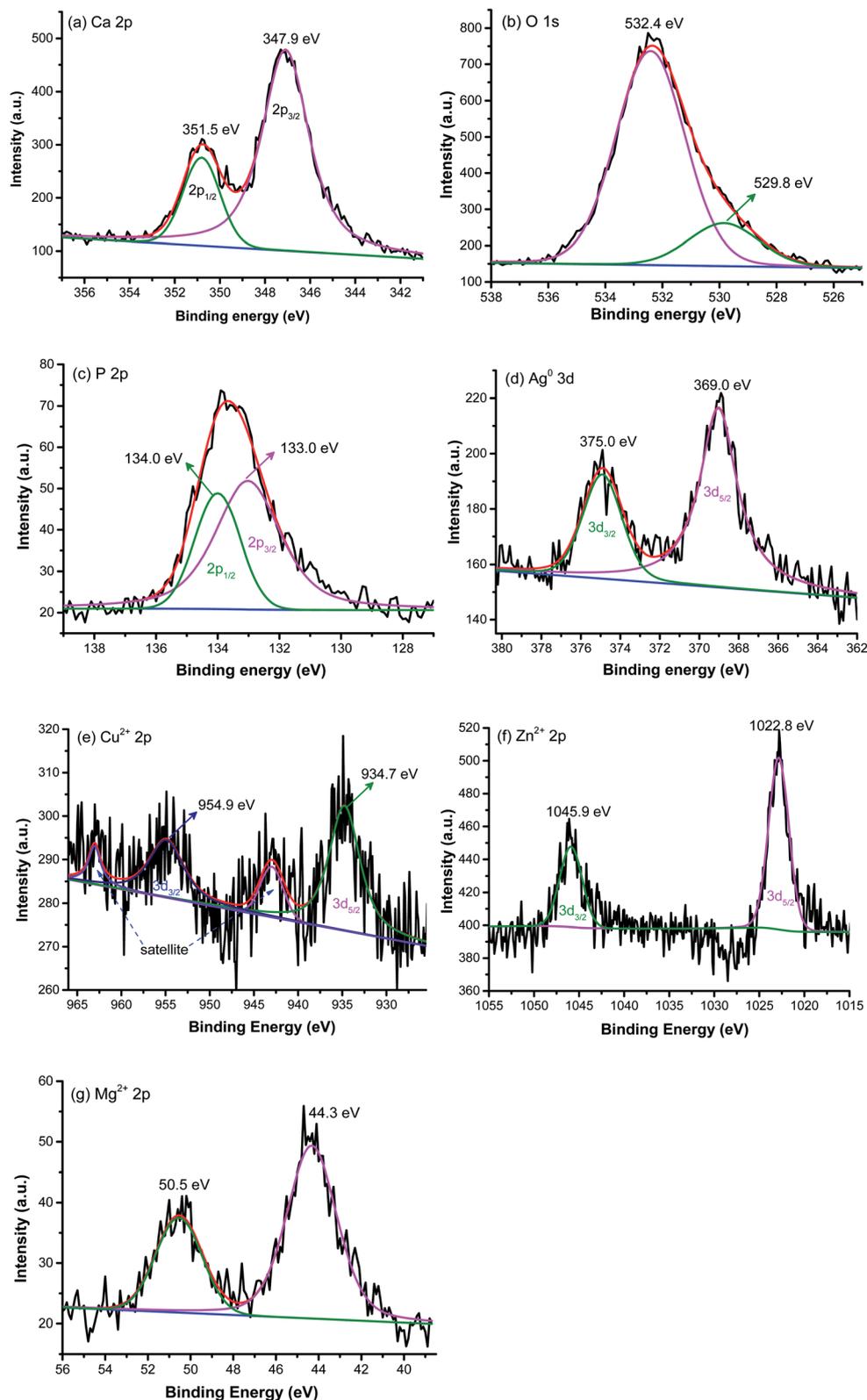
Fig. 4 X-ray photoelectron spectroscopy of pristine HAp (a) Ca, (b) O, (c) P and high-resolution of metal dopants (d) Ag, (e) Cu, (f) Zn, and (g) Mg.

at 934.7, 942.9, 954.9, and 963.0 eV correspond to the spin orbit of $2p_{3/2}$, a satellite of $2p_{3/2}$, spin orbit $2p_{1/2}$, and satellite of $2p_{1/2}$, respectively.[31] Those binding energies also state the presence of

bimetal copper (Cu^{2+}). Fig. 4f presents the high-resolution XPS for Zn^{2+} 2p, with a delta binding energy of 23.1 eV. The peak positions of Zn $2p_{3/2}$ and Zn $2p_{1/2}$ are located at 1022.8 and

Table 2 XPS composition of pristine, Ag-, Cu-, Zn-, and Mg-doped HAps

Samples	Metal ions dopant	Ca	P	O	(Ca + M)/P
HAp	—	17.23	10.27	72.48	1.68
Ag-HAp	0.90	16.84	10.02	72.24	1.68
Cu-HAp	0.95	16.73	10.52	71.80	1.68
Zn-HAp	1.08	16.80	10.62	71.50	1.68
Mg-HAp	0.80	16.90	10.50	71.80	1.68

1045.9 eV, respectively.[35] For as prepared Mg-doped HAp, the high resolution of Mg (Fig. 4g) exhibits two peaks at 50.5 and 44.3 eV that indicate the presence of Mg bonding with oxygen[36] and phosphate,[37] respectively.

Table 2 tabulates the concentration of calcium, phosphor, oxygen, and metal dopants for pristine and doped HAp based on XPS peak area and sensitivity factor. The pristine HAp had the concentration of Ca, P, and O were 17.25, 10.27, and 72.24%, respectively. With this composition, the ratio of Ca/P is 1.68 which is slightly higher than stoichiometric HAp (Ca/P = 1.67) and the pristine HAp is categorized as a non-stoichiometric HAp.[38] XPS composition analyses of Ag-HAp showed Ag, Ca, P and O were 0.90, 16.84, 10.02, and 72.24%, respectively. Similar to that un-doped HAp, the Ca/P ratio of Ag-HAp was also about 1.68. There is no significant difference of (Ca + M)/P ratio for Cu-, Zn-, and Mg-HAp compared to pristine and Ag-HAps.

3.4 Infrared spectra analyses

To confirm the functional group such as phosphate and hydroxide in pristine and doped-HAp, FT-IR analysis was

carried out and the result was shown in Fig. 5. There is no significant IR spectra difference for un-doped and Ag doped-HAp, indicating that Ag dopant does not enter the Ca^{2+} sides. For the rest of the metal ions dopant (Cu, Zn, Mg), a new and weak peak appears at a wavenumber of 940 cm^{-1}, as clearly shown in Fig. 5b. This peak provides evidence that those metal ions have been successfully doped into HAp.[39,40] Table 3 summarizes the band assignment of IR analyses. The peak located at a wavenumber of 1035 cm^{-1} is related to asymmetric stretching mode atom P and O in PO_4^{3-} functional group.[23] Furthermore, the peak at 940 cm^{-1} is also attributed to the active group of (PO_4^{3-}) with symmetric stretching (vibration mode of ν_1).[40,41] The observable peak at around 1455 cm^{-1} could be identified as the carbonate group (CO_3^{2-}). The functional group of carbonate might be attributed to the absorbed CO_2 on Ca sites as carbonate during the synthesis or during sample preparation of IR specimen. The carbonate has also appeared in HAp as stated in a previous report, even in the commercial powder.[42] The other broad peak at around 3500 cm^{-1} is assigned to the characteristic of OH^- stretching.[43] IR spectra results confirm that all as-prepared samples have the phosphate and hydroxide functional groups as hydroxyapatite material characteristics.

3.5 BET analysis

BET measurement was carried out to measure the surface area, pore size, and pore volume of un-doped and different metal ions doped HAp, and the result is shown in Table 4. The surface area of pristine HAp was only 21.91 m^2 g^{-1}. As expected, all the metal-doped HAps have a larger surface area than that of the pristine one. The surface areas of Ag-, Cu-, Zn-, and Mg-doped HAp are 30.51, 26.18, 27.88, and 26.98 m^2 g^{-1}, respectively.
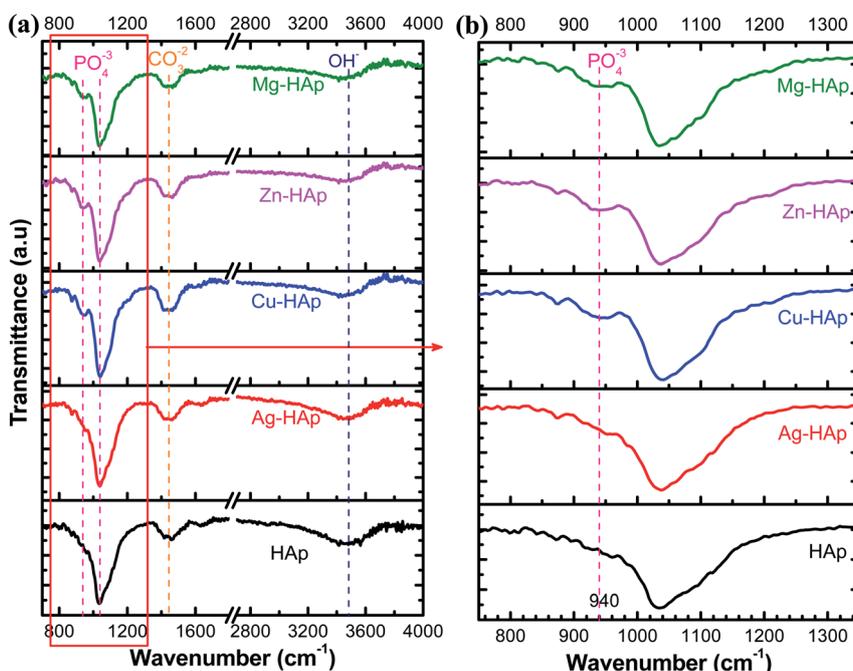

Fig. 5 IR spectra of pristine and Ag-, Cu-, Zn-, and Mg-doped HAps in different wavenumber regions (a and b).

Table 3 Peak assignment of FTIR analysis for pristine, Ag-, Cu-, Zn-, and Mg-doped HAps

HAp	Ag-HAp	Cu-HAp	Zn-HAp	Mg-HAp	Assignments
—	—	940	940	940	Symmetric stretching mode of PO_4^{3-}
1035	1038	1040	1036	1038	Asymmetric stretching mode of PO_4^{3-}
1460	1460	1462	1463	1464	CO_3^{2-}
3465	3470	3472	3470	3471	O–H stretching

Table 4 BET analyses of pristine, Ag-, Cu-, Zn-, and Mg-doped HAp

Sample name	Specific surface area ($m^2\ g^{-1}$)	Pore size (nm)	Pore volume (cc g^{-1})
HAp	21.91	1.57	0.03
Ag	30.51	1.57	0.04
Cu	26.18	1.57	0.04
Zn	27.88	1.73	0.03
Mg	26.98	1.57	0.03

Ag-doped HAp has the highest surface area with a 40% enhancement as compared to pure HAp. The rest metal ions doped HAp show a similar surface area with an improvement of about 22%. The enhancement of surface area was contributed by the smaller particle size of metal ions-doped HAp as depicted by SEM analysis in Fig. 2. The improved surface area after doping HAp was also reported in the previous works.[44] The higher surface area could be a favorite property to enhance the antibacterial rate since it will release more ions. The pore size did not significantly differ before and after being doped, except for Zn-doped HAp with a value of 1.73 nm was slightly more significant than other HAps. Similarly, the pore volume of pristine and metal-doped HAps did not alter with a size range of 0.03–0.04 cc g^{-1}.

3.6 Antibacterial activities

In this study, the nano HAp is doped with different metal ion dopants to improve and to compare their antibacterial activities against *E. coli* and *S. aureus* bacteria. Fig. S1† exhibits the photographic images of the antibacterial test after 24 h toward *E. coli* as an example for Gram-negative bacteria. As seen in Fig. S1b,† pristine HAp has a similar activity to the control one (Fig. S1a†). Interestingly, after doping with different metal ion dopants, their antibacterial performances are significantly improved, as shown in Fig. S1c–f.† The antibacterial ability is further calculated and the results are presented in Fig. 6a. The pristine HAp shows the activity of 4.4 ± 3.5%. Ag-HAp with a bactericidal percentage of 99.9 ± 0.1% exhibits the best antibacterial capability among the as-prepared HAp samples. The activity of our Ag-doped HAp was comparable to the previous reports that using synthetic chemical instead of natural source.[45,46] Zn-HAp with a bactericidal percentage of about 20.95 ± 2.11% shows the second-highest bactericidal activity and followed by Cu- and Mg-HAps with the activities of 13.28 ± 0.55% and 11.27 ± 1.29%, respectively. The

antibacterial activity of different metal ions doped HAp were also tested toward *S. aureus* to further evaluate their activities against Gram-positive bacteria. As exhibited in photograph images (see Fig. S2†), all metal doped HAps show a much better activity than that pristine HAp. Fig. 6b shows the histogram of activity of metal doped HAps toward *S. aureus*. The antibacterial rate of pristine, Ag-, Zn-, Cu-, and Mg-doped HAp are 10.23 ± 3.31, 99.9 ± 0.1, 69.44 ± 4.35, 55.55 ± 2.0, 54.62 ± 2.51, respectively. This antibacterial result also confirms the similar trend to that Gram negative where the highest activity with Ag-HAp followed by Zn-, Cu-, and Mg-HAps. Therefore, it is concluded that our metals doped HAp effectively to inactivate both *E. coli* and *S. aureus* bacteria.

3.7 Antibacterial mechanism

Based on the previous studies, there are two possible mechanisms of antibacterial mechanisms over metal ions-based
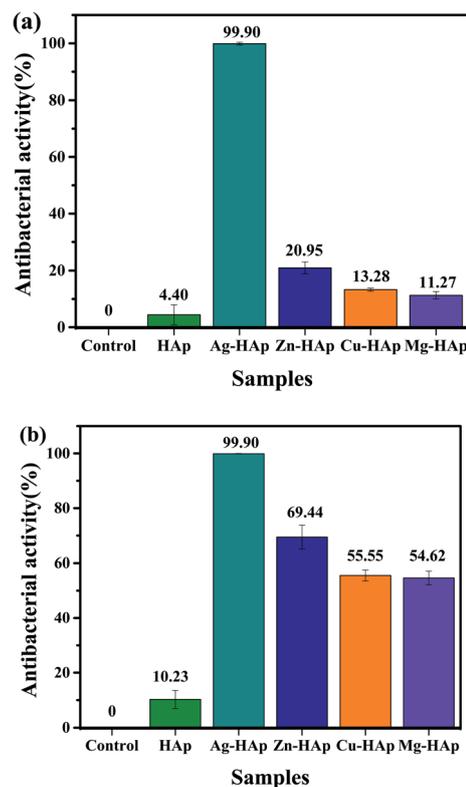

Fig. 6 Histogram of antibacterial activities toward (a) *E. coli* and (b) *S. aureus* in the presences of pristine HAp, Ag-, Cu-, Zn-, and Mg-HAps.

material. First, the direct contact between the bacterial wall with the metal ions (upon surface oxidation) *via* electrostatic interaction.[47] Second, disruption of the bacterial cell membrane by the formation of reactive oxygen species (ROS) such as superoxide ($O_2^{\cdot-}$), hydrogen peroxide (H_2O_2), and hydroxyl radical ($OH^{\cdot}$).[48,49] Antibacterial results show that pristine HAp only has a deficient antibacterial activity of about 4%, which perhaps due to Ca^{2+} ions releasing in the medium. However, after doping, the antibacterial remarkably improved, implying that metal ions' release is responsible for the improvement activity. The Ag-doped HAp was found to have the highest antibacterial activity among different metal ions doped HAp. This great activity could be attributed to several factors, including surface area which is a higher surface area increased the metal ion release.[50] Another reason is due to the monovalent of Ag which is Ag may be easier to release compared to the bivalent metal like Zn.[51] The death bacteria were analyzed using a scanning electron microscope to reveal the disruption of the wall membrane, as shown in Fig. S3.† It is clearly seen that the membrane is severely disruptive as indicated by the red arrows.

4. Conclusions

Nano-hydroxyapatite has been successfully synthesized using natural limestone as the calcium source. The broad of the XRD pattern confirms that as-prepared HAp possesses a small crystallite size. The particle size of HAp significantly decreases while surface area is greatly enhanced after being doped with different metal ion dopants. The capability of HAp to kill *E. coli* and *S. aureus* bacteria is also considerably improved after being doped with other metal ion dopants. The order of antibacterial activities are Ag-HAp > Zn-HAp > Cu-HAp > Mg-HAp > pristine HAp. The better antibacterial performance of metal-doped HAp is due to their ions released as elucidating in the antibacterial mechanism. This work not only demonstrates the utilization of earth-abundant natural limestone to synthesize nanohydroxyapatite but also investigates the effects of different metals doping to improve the antibacterial performance of HAp.

Conflicts of interest

The authors declare that there is no conflict interest in this work.

Acknowledgements

References

1 M. Akram, R. Ahmed, I. Shakir, W. A. W. Ibrahim and R. Hussain, *J. Mater. Sci.*, 2014, **49**, 1461–1475.

2 N. Lertcumfu, P. Jaita, S. Manotham, P. Jarupoom, S. Eitssayeam, K. Pengpat and G. Rujijanagul, *Ceram. Int.*, 2016, **42**, 10638–10644.

3 G. M. Raghavendra, K. Varaprasad and T. Jayaramudu, in *Nanotechnology Applications for Tissue Engineering*, ed. S. Thomas, Y. Grohens and N. Ninan, William Andrew Publishing, Oxford, 2015, DOI: 10.1016/B978-0-323-32889-0.00002-9, pp. 21–44.

4 J. Fang, P. Li, X. Lu, L. Fang, X. Lü and F. Ren, *Acta Biomater.*, 2019, **88**, 503–513.

5 E. Pepla, L. K. Besharat, G. Palaia, G. Tenore and G. Migliau, *Journal*, 2014, **5**, 108–114.

6 M. Sadat-Shojai, M.-T. Khorasani, E. Dinpanah-Khoshdargi and A. Jamshidi, *Acta Biomater.*, 2013, **9**, 7591–7621.

7 C. H. Yeo, S. H. S. Zein, A. L. Ahmad and D. S. McPhail, *Braz. J. Chem. Eng.*, 2012, **29**, 147–158.

8 M. A. Giardina and M. A. Fanovich, *Ceram. Int.*, 2010, **36**, 1961–1969.

9 M. Z. A. Khiri, K. A. Matori, N. Zainuddin, C. A. C. Abdullah, Z. N. Alassan, N. F. Baharuddin and M. H. M. Zaid, *SpringerPlus*, 2016, **5**, 1206.

10 L. Ćurković, I. Žmak, S. Kurajica, M. E. Tonković, Z. Šokčević and M. M. Renjo, *Materialwiss. Werkstofftech.*, 2017, **48**, 797–802.

11 M. M. H. Al Omari, I. S. Rashid, N. A. Qinna, A. M. Jaber and A. A. Badwan, in *Profiles of Drug Substances, Excipients and Related Methodology*, ed. H. G. Brittain, Academic Press, 2016, vol. 41, pp. 31–132.

12 I. S. Neira, Y. V. Kolen'ko, O. I. Lebedev, G. Van Tendeloo, H. S. Gupta, F. Guitián and M. Yoshimura, *Cryst. Growth Des.*, 2009, **9**, 466–474.

13 M. Safari Gezaz, S. Mohammadi Aref and M. Khatamian, *Mater. Chem. Phys.*, 2019, **226**, 169–176.

14 M. Salari, S. Mohseni Taromsari, R. Bagheri and M. A. Faghihi Sani, *J. Mater. Sci.*, 2019, **54**, 4259–4276.

15 S. Türk, I. Altınsoy, G. Çelebi Efe, M. Ipek, M. Özacar and C. Bindal, *Mater. Sci. Eng., C*, 2018, **92**, 757–768.

16 R. Ying, H. Wang, R. Sun and K. Chen, *Mater. Sci. Eng., C*, 2020, **110**, 110689.

17 L.-J. Fuh, Y.-J. Huang, W.-C. Chen and D.-J. Lin, *Mater. Sci. Eng., C*, 2017, **75**, 798–806.

18 D. Predoi, S. L. Iconaru, M. V. Predoi, G. E. Stan and N. Buton, *Nanomaterials*, 2019, **9**, 1295.

19 S. Samani, S. M. Hossainalipour, M. Tamizifar and H. R. Rezaie, *J. Biomed. Mater. Res., Part A*, 2013, **101A**, 222–230.

20 Y.-J. Chou, H. S. Ningsih and S.-J. Shih, *Ceram. Int.*, 2020, **46**, 16708–16715.

21 B. Gayathri, N. Muthukumarasamy, D. Velauthapillai, S. B. Santhosh and V. asokan, *Arabian J. Chem.*, 2018, **11**, 645–654.

22 M. Riaz, R. Zia, A. Ijaz, T. Hussain, M. Mohsin and A. Malik, *Mater. Sci. Eng., C*, 2018, **90**, 308–313.

23 E. A. Ofudje, A. I. Adeogun, M. A. Idowu and S. O. Kareem, *Heliyon*, 2019, **5**, e01716.

24 S. Kamonwannasit, C. M. Futalan, P. Khemthong, T. Butburee, A. Karaphun and P. Phatai, *J. Sol-Gel Sci. Technol.*, 2020, **96**, 452–463.

25 V. Stanic, S. Dimitrijevic-Brankovic, J. Stankovic, M. Mitrić, B. Jokic, I. Plećaš and S. Raičević, *Appl. Surf. Sci.*, 2010, **256**, 6083–6089.

26 D. Gopi, E. Shinyjoy and L. Kavitha, *Spectrochim. Acta, Part A*, 2014, **127**, 286–291.

27 A. Jacobs, M. Gaulier, A. Duval and G. Renaudin, *Crystals*, 2019, **9**, 326.

28 S. Jadalannagari, K. Deshmukh, S. R. Ramanan and M. Kowshik, *Appl. Nanosci.*, 2014, **4**, 133–141.

29 D.-H. Kuo, H. Abdullah, N. S. Gultom and J.-Y. Hu, *ACS Appl. Mater. Interfaces*, 2020, **12**, 35011–35021.

30 Y. Yang, H. Wang, F.-Y. Yan, Y. Qi, Y.-K. Lai, D.-M. Zeng, G. Chen and K.-Q. Zhang, *ACS Appl. Mater. Interfaces*, 2015, **7**, 5634–5642.

31 W. F. S. J. F. Moulder, P. E. Sobol and K. D. Bomben, *Handbook of X-Ray Photoelectron Spectroscopy*, Physical Electronic Inc, Eden Prairie, 1995.

32 N. Zhang, H. Xue and R. Hu, *RSC Adv.*, 2018, **8**, 32922–32929.

33 G. C. Gomes, F. F. Borghi, R. O. Ospina, E. O. López, F. O. Borges and A. Mello, *Surf. Coat. Technol.*, 2017, **329**, 174–183.

34 H. Abdullah, N. S. Gultom and D.-H. Kuo, *J. Mater. Sci.*, 2017, **52**, 6249–6264.

35 N. S. Gultom, H. Abdullah and D. H. Kuo, *Int. J. Hydrogen Energy*, 2019, **44**, 29516–29528.

36 B. A. Taleatu, E. Omotoso, C. Lal, W. O. Makinde, K. T. Ogundele, E. Ajenifuja, A. R. Lasisi, M. A. Eleruja and G. T. Mola, *Surf. Interface Anal.*, 2014, **46**, 372–377.

37 Y. Song, D. Shan, R. Chen, F. Zhang and E.-H. Han, *Corros. Sci.*, 2009, **51**, 62–69.

38 H. Esfahani, E. Salahi, A. Tayebifard, M. R. Rahimipour and M. Keyanpour-Rad, *Matéria*, 2016, **21**, 569–576.

39 I. Uysal, F. Severcan and Z. Evis, *Ceram. Int.*, 2013, **39**, 7727–7733.

40 S. Gomes, J.-M. Nedelec, E. Jallot, D. Sheptyakov and G. Renaudin, *Chem. Mater.*, 2011, **23**, 3072–3085.

41 D. Rabadjieva, S. Tepavitcharova, R. Gergulova, K. Sezanova, R. Titorenkova, O. Petrov and E. Dyulgerova, *J. Mater. Sci.: Mater. Med.*, 2011, **22**, 2187.

42 L. Berzina-Cimdina and N. Borodajenko, *Research of Calcium Phosphates Using Fourier Transform Infrared Spectroscopy*, IntechOpen, London, UK, 2012, p. 127, DOI: 10.5772/36942.

43 F. Bollino, E. Armenia and E. Tranquillo, *Materials*, 2017, **10**, 757.

44 G. Karunakaran, E.-B. Cho, G. S. Kumar, E. Kolesnikov, G. Janarthanan, M. M. Pillai, S. Rajendran, S. Boobalan, M. V. Gorshenkov and D. Kuznetsov, *ACS Appl. Bio Mater.*, 2019, **2**, 2280–2293.

45 M. Jelinek, T. Kocourek, J. Remsa, M. Weiserová, K. Jurek, J. Mikšovský, J. Strnad, A. Galandáková and J. Ulrichová, *Mater. Sci. Eng., C*, 2013, **33**, 1242–1246.

46 M. Mirzaee, M. Vaezi and Y. Palizdar, *Mater. Sci. Eng., C*, 2016, **69**, 675–684.

47 S. Ghosh, V. S. Goudar, K. G. Padmalekha, S. V. Bhat, S. S. Indi and H. N. Vasan, *RSC Adv.*, 2012, **2**, 930–940.

48 Q. L. Feng, J. Wu, G. Q. Chen, F. Z. Cui, T. N. Kim and J. O. Kim, *J. Biomed. Mater. Res.*, 2000, **52**, 662–668.

49 J. A. Imlay, S. M. Chin and S. Linn, *Science*, 1988, **240**, 640–642.

50 Y. X. Hou, H. Abdullah, D. H. Kuo, S. J. Leu, N. S. Gultom and C. H. Su, *Composites, Part B*, 2018, **133**, 166–176.

51 Y. Jin, Z. Dai, F. Liu, H. Kim, M. Tong and Y. Hou, *Water Res.*, 2013, **47**, 1837–1847.